Effectiveness of an RbF Post Deposition Treatment of CIGS Solar Cells in Dependence on the Cu Content of the Absorber Layer

Tim Kodalle, Tobias Bertram, Rutger Schlatmann, and Christian A. Kaufmann

***Abstract*—In this contribution, the effectiveness of an RbF post deposition treatment (PDT) is evaluated in dependence on the Cu content of the absorber layer of $Cu(In,Ga)Se_2$ solar cells. It is shown that the PDT only acts beneficially on the open-circuit voltage and fill factor (*FF*) on samples with rather high Cu content, while it deteriorates all parameters of the solar cells in samples with low Cu content. In order to clarify the behavior of the open-circuit voltage, the well-known exchange mechanism of Rb and Na during the PDT is analyzed as a function of the Cu content of the absorber layers and discussed in regard to theoretical publications. Furthermore, a model explaining the observed effect on the FF based on the formation of an $RbInSe_2$ (RIS) layer during the RbF-PDT is proposed. The model supposes that the RIS layer acts as a barrier for the photocurrent and therefore lowers the *FF*. It is evaluated theoretically in dependence of the properties of the RIS layer using one-dimensional solar cell capacitance simulator (SCAPS) simulations. Finally, the proposed model is also tested and confirmed experimentally by directly depositing RIS onto untreated $Cu(In,Ga)Se_2$ layers.**

***Index Terms*—$Cu(In,Ga)Se_2$ (CIGS) solar cells, heavy alkali metals, RbF-PDT, $RbInSe_2$ (RIS).**

I. Introduction

In RECENT years, the implementation of heavy alkali post deposition treatments (PDTs) into the deposition procedure of thin film solar cells based on $Cu(In,Ga)Se_2$ (CIGS) absorber layers has led to significant improvements of the power conversion efficiency (η) of this type of solar cells [1]–[3]. Generally, the improvement of η of a device due to a PDT is mostly attributed to a gain in open circuit voltage (V_{OC}) and the opportunity to decrease the thickness of the buffer layer resulting in enhanced short-circuit current density (j_{SC}) [1]. However, both gain and loss in fill factor (*FF*) due to the PDTs have been reported [1]–[5]. The reason for these different trends remains unclear so far. While this behavior is valid for high-efficiency devices, for which absorber layers are usually grown with a Ga to In ratio ([Ga]/([Ga] + [In]) = *GGI*) of about 0.3, it was reported by Ishizuka *et al.* [6] as well as Zahedi-Azad *et al.* [7] that the effectiveness of the PDTs depends on *GGI*. While the PDTs increase all device parameters in samples with $GGI \approx 0.75$ [7], no performance improvements were achieved on samples with $GGI = 1$ [6]. Moreover, there is a study by Lepetit *et al.* [8] stating that an KF-PDT leads to deterioration of the device parameters on samples with a Cu to In and Ga ratio ([Cu]/([Ga] + [In]) = *CGI*) close to 1 and is only beneficial on samples with rather low *CGI*. However, to the best of our knowledge, no systematical study investigating the effectiveness of such a PDT in dependence on the *CGI* has been conducted yet.

In this contribution, we are examining the impact of an RbF-PDT on devices with *CGI* ranging from 0.45 up to $CGI = 0.95$. Contrary to the results published by Lepetit *et al.* we find that the RbF-PDT only improves all device parameters on samples grown close to stoichiometry, whereas on samples with low *CGI* all device parameters are decreased. We analyze the impact of the PDT on the devices using current density–voltage (j–V) as well as capacitance–voltage (C–V) measurements, Raman scattering, and glow discharge optical emission spectroscopy (GD-OES). Furthermore, we propose a model explaining the observed trends based on device simulations. To test this model, which attributes the observed trend in *FF* to the formation of $RbInSe_2$ (RIS) at the surface of the CIGS during the PDT, we evaluate the effect of a direct coevaporation of RIS on top of CIGS with $CGI = 0.95$.

II. Experimental

For the *CGI* variation, ten deposition processes resulting in samples with five different *CGI* (with and without *in situ* RbF-PDT) were performed via thermal coevaporation using a three-stage process on Mo-covered soda-lime glass. The highest substrate temperature during the deposition process was set to 530 °C. In case of samples with RbF-PDT, it was performed right after finishing the growth of the CIGS without breaking the vacuum. The PDT consists of the coevaporation of RbF and Se for 10 min at a substrate temperature of 280 °C (nominal RbF thickness is about 10 nm) and a subsequent annealing step at the same temperature for 5 min without additional evaporation of RbF or Se. More details of the deposition process are described

Manuscript received June 3, 2019; revised July 10, 2019; accepted July 11, 2019. Date of publication August 9, 2019; date of current version October 28, 2019. *(Corresponding author: Tim Kodalle.)*

T. Kodalle, T. Bertram, and C. A. Kaufmann are with the Helmholtz-Zentrum Berlin für Materialien und Energie GmbH, Berlin 14109, Germany (e-mail: tim.kodalle@helmholtz-berlin.de; tobias.bertram@helmholtz-berlin.de; kaufmann@helmholtz-berlin.de).

R. Schlatmann is with the Helmholtz-Zentrum Berlin für Materialien und Energie GmbH, Berlin 14109, Germany, and also with the Hochschule für Technik und Wirtschaft Berlin, Berlin 10318, Germany (e-mail: rutger.schlatmann@helmholtz-berlin.de).

Color versions of one or more of the figures in this paper are available online at http://ieeexplore.ieee.org.

Digital Object Identifier 10.1109/JPHOTOV.2019.2929418

This work is licensed under a Creative Commons Attribution 4.0 License. For more information, see https://creativecommons.org/licenses/by/4.0/

TABLE I
PARAMETERS USED FOR THE SCAPS SIMULATIONS

Property	CIGS	CdS	ZnO	RIS
E_g [eV]	from GD-OES	2.4	3.3	2.8
W [eV]	from GD-OES	4.3	4.45	varied
d [nm]	from GD-OES	60	150	varied
n/p [cm^{-3}]	$p = 5.5 \cdot 10^{15}$	$n = 1 \cdot 10^{16}$	$n = 1 \cdot 10^{19}$	$n = 1 \cdot 10^{14}$
α [cm^{-1}]	from UV-Vis	$\sqrt{h\nu - E_g}$	from UV-Vis	from UV-Vis
Neutral (Gaussian) Defect States				
N_D [cm^{-3}]	$1 \cdot 10^{14}$	$1.8 \cdot 10^{18}$	$1.8 \cdot 10^{16}$	-
w_D [eV]	Single Defect	0.1	0.1	-
E_D [eV]	0.6 above VB	Midgap	Midgap	-
σ_e [cm^2]	$1 \cdot 10^{14}$	$1 \cdot 10^{-13}$	$1 \cdot 10^{-12}$	-
σ_h [cm^2]	$1 \cdot 10^{15}$	$1 \cdot 10^{-13}$	$1 \cdot 10^{-12}$	-

in [9]. The variation of the *CGI* was implemented by adapting the duration of the third stage using laser-light scattering (LLS) [10].

For the second part of the study, we performed six additional CIGS depositions with $CGI = 0.95$. While one of the absorber runs was kept free of Rb, we deposited RIS on top of the absorbers of the other five runs. The thickness of the deposited RIS was varied from nominally 5 nm (1 min RIS) to up to 30 nm (6 min RIS). The RIS was deposited at a substrate temperature of 530 °C using the same procedure as it is described in [11]. Solar cells were completed by adding a chemical bath deposited CdS buffer layer (nominal thickness: 60 nm) as well as a bilayer of undoped and Al-doped ZnO (RF-sputtered), and, finally, an electron beam evaporated Ni–Al–Ni contact grid.

Raman scattering was measured using a setup based on components by Spectroscopy & Imaging GmbH equipped with a laser emitting light at a wavelength of $\lambda = 532$ nm, resulting in an information depth of about 100–150 nm. GD-OES measurements were performed using a Spectruma GDA 650 and quantified using the procedure described in [12]. In order to determine the optical bandgap and to be able to calculate the V_{OC}-deficit, the external quantum efficiency (*EQE*) was measured using a self-built setup. The optical bandgap was then derived using the maximum of the derivative of the EQE. Simulations were carried out using SCAPS-1D [13]. The model, which consists of a spike between the CIGS and the CdS layer (60 meV), is using actual GD-OES and C–V data for bandgap grading and the carrier concentration within the CIGS layer, respectively. All relevant parameters are summarized in Table I or, if not shown there, were taken from the work presented in [14]. In the table, E_g denotes the bandgap energy, W the work function, d the thickness, n and p the charge carrier concentrations, α the absorption coefficient, N_D the defect density, w_D the width of the defect distribution, E_D the energetic position of the defects, and σ_e and σ_h the capture cross sections of the electrons and holes for the respective layers. Furthermore, a neutral, single interface defect was positioned at $E_D = 0.6$ eV above the lowest valence band (VB) at the absorber/buffer interface.

III. EFFECTIVENESS OF THE RbF-PDT IN DEPENDENCE ON THE CGI

A. Effects on V_{OC}

Due to the fact that the variation of the *CGI* was achieved by changing the duration of stage 3, the CIGS layers are not only different in *CGI* but also in their thickness, E_g-grading as

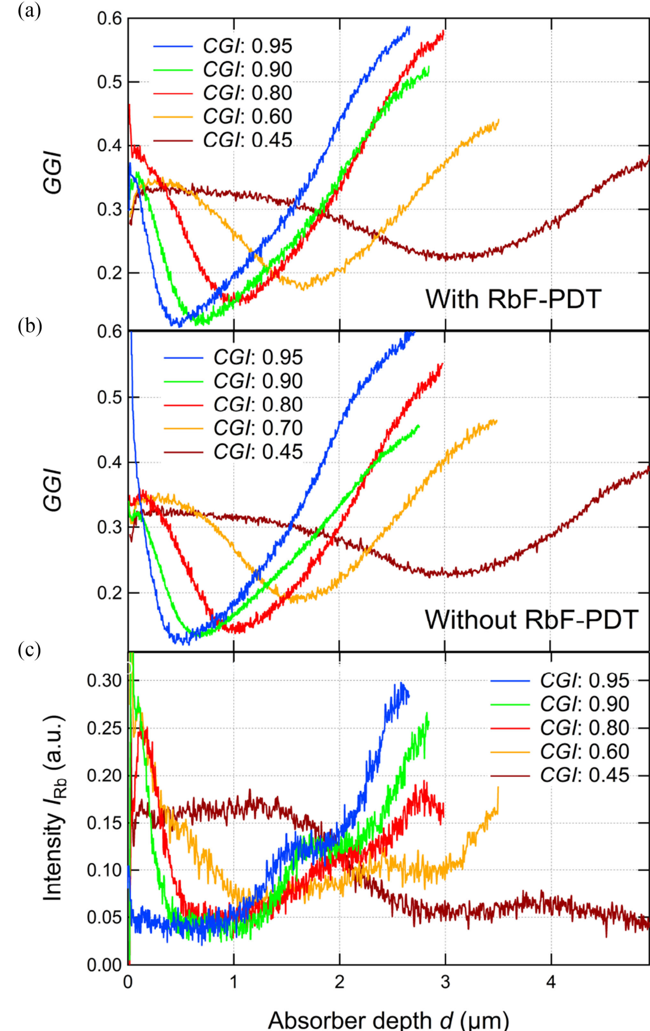

Fig. 1. (a) GD-OES depth profiles of the *GGI* of the samples with RbF-PDT. (b) Depth profiles of the *GGI* of the samples without RbF-PDT. The profiles are in good agreement with the ones of the samples without PDT, ensuring the comparability. (c) Distribution of Rb in these samples as measured by GD-OES. Note that these profiles are showing the unquantified intensities of the Rb signal, since we do not have a reference sample for the quantification of the Rb signal. To ensure comparability, all profiles were measured on the same day.

well as the position and value of the minimum E_g. However, all these variations are the same for the sample set with and without RbF-PDT ensuring the comparability of both samples with the same *CGI* each [cf. Fig. 1(a) and (b)]. To take these deviations into account when judging the effectiveness of the PDT, the V_{OC}-deficit ($\Delta V_{OC} = E_g/q - V_{OC}$) of all samples is shown in Fig. 2(a) in addition to their PV parameters, which are listed in Table II. In the table, headers *CGI* (LLS) describes the *CGI* we aimed for during the deposition, t_{III} describes the duration of the third stage, and *CGI* describes the values measured by energy-dispersive X-ray spectroscopy using a scanning electron microscope (SEM-EDX) at an acceleration voltage of 20 kV.

As can be seen in Fig. 2(a) and Table II, the RbF-PDT is increasingly effective with higher *CGI*. While it lowers all parameters on samples with very low *CGI*, it leads to a benefit

TABLE II
PROCESS DETAILS AND *PV* PARAMETERS IN DEPENDENCE ON THE *CGI* OF THE CIGS ABSORBER LAYERS

CGI (LLS)	t_{III} (s)	*CGI* (at%)	*GGI* (at%)	RbF	PV-Parameters j_{SC} (mA/cm^2)	V_{OC} (mV)	*FF* (%)	η (%)
0.45	5300	0.46	0.36	no	22.1	585	52.0	6.7
0.45	5300	0.45	0.36	yes	15.0	443	48.3	3.2
0.6	2275	0.61	0.36	no	32.9	630	70.0	14.5
0.6	2260	0.63	0.35	yes	32.9	570	66.9	12.5
0.8	1228	0.81	0.31	no	34.6	650	71.6	16.1
0.8	1241	0.79	0.34	yes	33.9	676	68.6	15.7
0.9	685	0.90	0.24	no	34.9	647	72.6	16.4
0.9	669	0.87	0.27	yes	35.1	675	71.5	17.0
0.95	365	0.94	0.24	no	34.3	656	72.8	16.4
0.95	411	0.95	0.24	yes	34.2	684	74.5	17.5

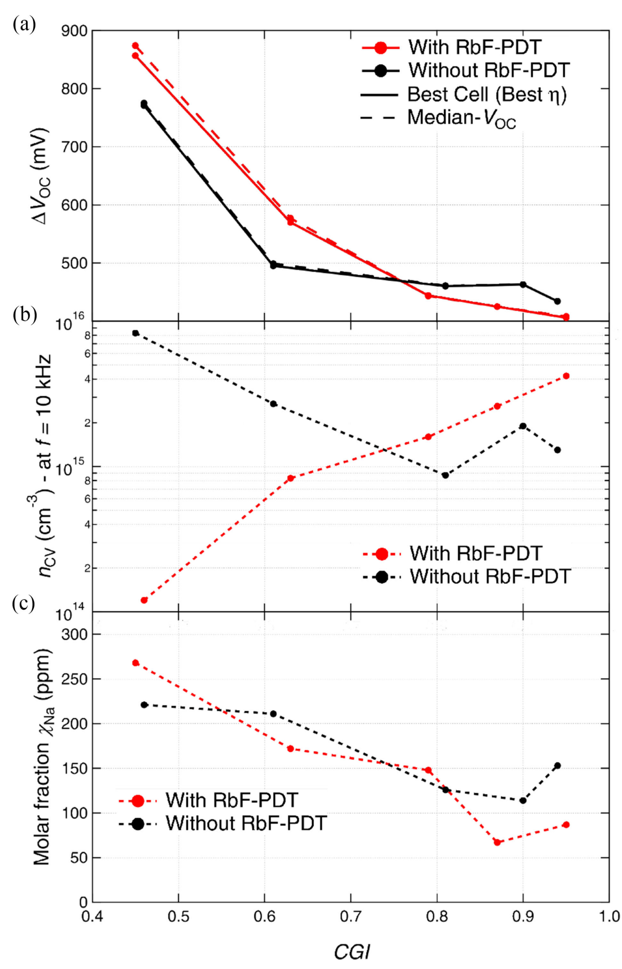

Fig. 2. (a) ΔV_{OC} of the most efficient cell as well as the cell with the median V_{OC} of each sample plotted versus the *CGI*. (b) Evolution of n_{CV} with CGI as measured by C–V profiling. (c) Molar fraction of Na in dependence of the *CGI* of the absorber layer (as measured by GD-OES).

in V_{OC} and ΔV_{OC} at $CGI \gtrsim 0.8$. Fig. 2(b) shows the majority carrier concentration as measured by C–V profiling (n_{CV}). While n_{CV} of the untreated devices shows a slightly decreasing trend with higher *CGI*, n_{CV} of RbF-treated devices is rising steadily. Therefore, the RbF-PDT leads to lower n_{CV} in samples with $CGI < 0.8$ and to higher n_{CV} in samples with $CGI \geq 0.8$. This is the same trend as observed for ΔV_{OC}. In Fig. 2(c), the molar fraction of Na (χ_{Na}) versus the *CGI* is displayed. A Na–Rb exchange mechanism, that is widely discussed in literature for samples with $CGI \approx 0.9$ [15]–[18], is apparently only valid in samples with such high *CGI* (>0.8). On samples with lower *CGI*, χ_{Na} of treated and untreated samples is comparable, indicating that the RbF-PDT does not lead to an out-diffusion of Na in these samples. This poses the question if there is also no Rb-induced diffusion of Na into the grain interior taking place as it was described for CIGS grown close to stoichiometry [15]. The latter could explain the rather low n_{CV} measured on RbF-treated devices with low *CGI*, and therefore also the observed trend in ΔV_{OC}. Note that we did not observe a trend in grain size of the samples when changing the *CGI* (not shown), and therefore assume that the differences observed in the alkali distribution and amount are not due to variations in morphology. Furthermore, it is interesting to note that the Na content in both samples with $CGI = 0.95$ is slightly higher than the one of the samples with $CGI = 0.90$. This is surprising, since a negative correlation of the Cu and Na contents in Rb-free samples would be expected based on literature [20]. We therefore assume that this slight increase is just due to the error of the measurement.

B. Effects on FF

The RbF-PDT only leads to an improved *FF* on samples grown at $CGI = 0.95$. The *FF* loss due to the RbF-PDT on the other samples gets larger with lower *CGI*. In Fig. 1(b), elemental depth profiles of Rb measured on the RbF-treated sample set are shown. One can see that Rb accumulates near the absorber surface as well as at the back side of the absorber. The latter is attributed to an agglomeration of Rb in between the CIGS and the $MoSe_2$ layer, as it was already reported by Schoeppe *et al.* [19]. Since samples with higher *CGI* are thinner, more Rb could diffuse along the grain boundaries (GBs) to the back contact compared with samples with lower *CGI*. This explains why the accumulation there gets bigger with increasing *CGI*. The accumulation of Rb at the surface of the absorber layer, however, extends deeper into the absorber layer the lower the *CGI* is. Note that all profiles were measured on absorbers, which have been rinsed in NH_4OH, ensuring that the observed accumulations represent either Rb incorporated into the lattice of the CIGS

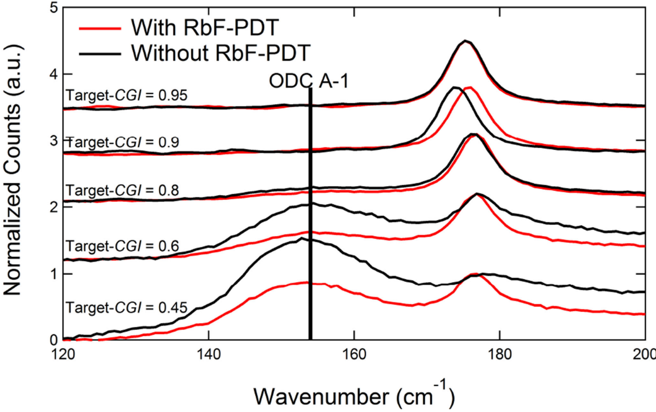

Fig. 3. Raman spectra of the samples with and without PDT in dependence on the *CGI*. All spectra were normalized to the CIGS A1 mode.

or a secondary phase growing on top of the CIGS during the PDT. We could show in earlier work that the RbF-PDT leads to the formation of a secondary surface phase containing Rb, Na, In, and Se [16]. Furthermore, we could show that the most likely candidate for this phase is RIS [21], which is an n-type semiconductor with a bandgap energy of about 2.8 eV [11]. The depth profiles in Fig. 1(b) suggest that the thickness of this RIS layer increases with decreasing *CGI*.

In order to investigate the formation mechanism of the RIS layer in more detail, Raman spectra of this sample set are shown in Fig. 3. On samples with *CGI* ≤ 0.8, there is a clear contribution of the A1 mode of the so-called ordered defect compound (ODC) visible in the spectra (at wavenumbers of $k \approx 154\,\mathrm{cm}^{-1}$ [22]). In all cases, the intensity of the ODC is reduced by the RbF-PDT, indicating that the Cu-poor ODC phase is partly consumed during the PDT. Including the depth profiles displayed in Fig. 1(b), we conclude that the presence of a thicker ODC phase at the surface of the CIGS leads to the formation of a thicker RIS phase during the PDT and a stronger reduction of *FF*.

Combining all the results described above, we propose that the interaction of the *CGI* with the effect of the RbF-PDT on both, V_{OC} and *FF*, is related to the interaction of Rb, Na, and the available amount of Cu vacancies ($\mathrm{V_{Cu}}$) in the CIGS lattice. The positive effect of Rb on V_{OC} is—among other mechanisms—generally attributed to the following effects: an Rb–Na exchange mechanism, in which Rb pushes Na into the grain interior leading to improved n_{CV} [15]–[18] as well as a subsequent passivation of the GBs by the Rb itself [19]–[24] leading to improved carrier lifetimes [3], [18], [25]. On the other hand, recently published Monte Carlo simulations show that for heavy alkali metals (like Rb) the diffusion via $\mathrm{V_{Cu}}$ has much lower energy barriers than diffusion via interstitial positions in the lattice, while in case of Na these barriers are comparable [26]. Therefore, it seems likely that Rb preferably occupies Cu sites in Cu-poor material near the GBs or at the surface of the CIGS [26], but is rather unlikely to replace Cu in a stoichiometric CIGS lattice. In samples with a high number of available $\mathrm{V_{Cu}}$, Rb may hence not occupy Na sites at the GBs but directly diffuses into the Cu-poor material at the surface of the CIGS lattice [cf. Figs. 1(b) and 3]. As a consequence, in samples with high *CGI* (low amount of $\mathrm{V_{Cu}}$), an RbF-PDT would not lead to the Na–Rb exchange mechanism or the GB passivation described earlier. We propose that this is the reason why the PDT does not increase the V_{OC} on samples with *CGI* < 0.8, but only on samples with higher CGI. At the same time this accumulation of Rb at the surface of the CIGS layer leads to the formation of an RIS layer [16], [21], whose thickness is dependent on the *CGI* as well. Accordingly, we conclude that the ODC is part of the formation mechanism of the RIS, and that the formation of the RIS can in turn be suppressed by limiting the amount of the ODC, e.g., the number of available $\mathrm{V_{Cu}}$ at the surface.

This behavior stands—as it was already mentioned—in contrast with the results of Lepetit *et al.* [8] regarding KF-PDTs, where they concluded that in samples grown close to stoichiometry, K atoms are still diffusing into the surface area of the CIGS leading to an out-diffusion of Cu, the formation of detrimental $\mathrm{Cu_{2-x}Se}$, and therefore strongly reduced performance of the devices [8]. The reason why we do not see this behavior in case of the RbF-PDT can be found in the literature. While the formation energy of K- and Rb-related point defects at GBs are comparable, K is predicted to be more likely to diffuse into the grain interior than Rb [24], [27]. In case of samples grown close to stoichiometry, this means that Rb is more prone to remain at GBs by displacing Na, most likely pushing it into the grains improving the V_{OC} as described earlier. Residual Rb, however, stays at the surface of the CIGS and is rinsed off by $\mathrm{NH_4OH}$ and does therefore only lead to the formation of a very thin or no RIS layer at the surface. Formation of $\mathrm{Cu_{2-x}Se}$ does not occur. This is in good agreement with the fact that samples with *CGI* $= 0.95$ neither show a detectable ODC A1-mode nor the accumulation of the alkali metals at the surface (see Fig. 3). Without a RIS layer being present, the *FF* increases with increasing V_{OC} just as one would expect. This interpretation, however, implies that the presence of the RIS layer is the reason for the observed drop of *FF* in samples with *CGI* < 0.95.

SCAPS simulations show that the introduction of a high-E_{g} layer, just as RIS, in between the CIGS and the CdS can lead to a barrier for the electrons. This barrier reduces *FF* compared with the device without RIS (cf. Fig. 4). The simulations show that the *FF* loss gets more pronounced with increasing thickness of the RIS supporting the model and that the increasingly thick RIS formation on samples with lower *CGI* leads to the observed trend in *FF*. Please note that there are some unknown input parameters of the RIS layer, like e.g., its doping, defects, position of the conduction band minimum (CBM), and actual thickness. While the influence of the CBM offset (ΔCBM is the difference of the CBM of the RIS and the CdS layer) is shown in Fig. 4, the influence of the doping and the defects are not shown here. However, all realistic parameter combinations we tested so far, lead to an increasing loss in *FF* with increasing RIS thickness. Note that we assumed the RIS layer to be highly resistive, since its conductivity is below the detection limit of our setup.

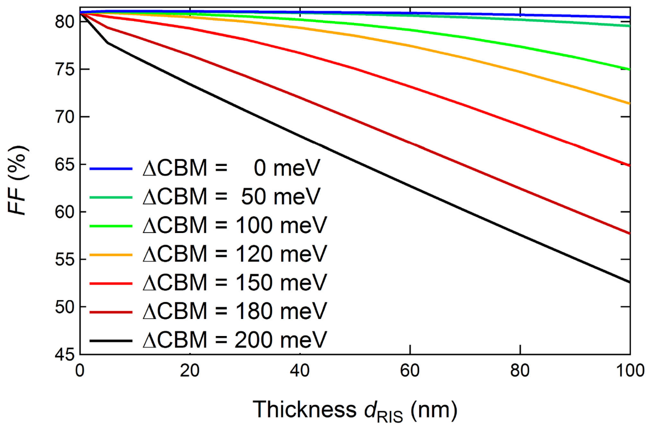

Fig. 4. Evolution of *FF* in dependence of the thickness of the RIS layer and the line-up of its CBM with the one of the CdS buffer layer.

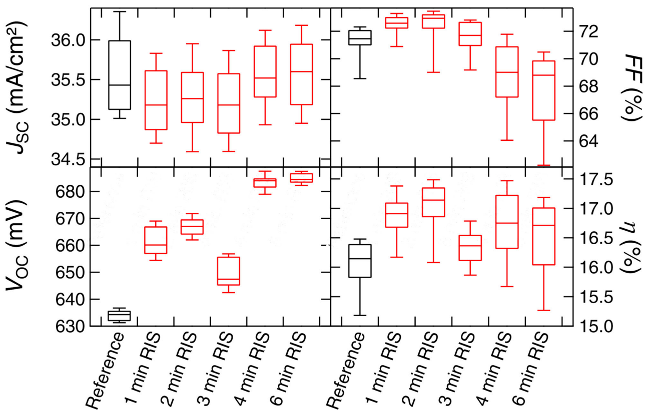

Fig. 6. Boxplots of the PV parameters of 45 cells per box in dependence of the deposition duration of the RIS. The V_{OC} of the sample "3 min RIS" is reduced due to handling issues.

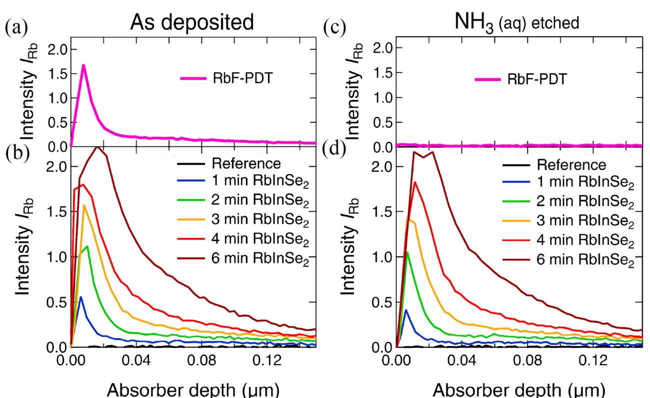

Fig. 5. Rb-depth profiles as measured by GD-OES. (a) and (b) Measured directly after deposition. (c) and (d) Measured after rinsing the samples in diluted ammonia. Please note that the Rb intensity after rinsing (c) does only appear to be lower than the corresponding value in Fig. 1(b) because of the different scales of the axis used in the figures.

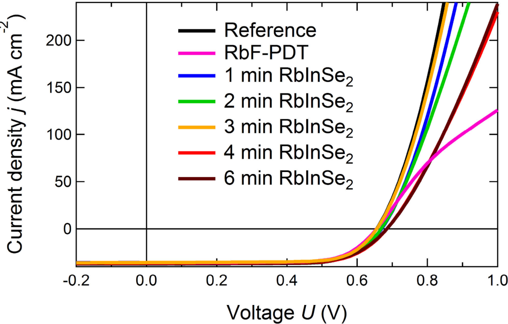

Fig. 7. j–V curves of the best cell of each sample set.

IV. Testing the RIS Model Experimentally

Following the model described earlier, the *FF* loss does not occur for cells with absorber layers grown with $CGI = 0.95$, because this composition does not lead to sufficient Cu deficiency at the surface of the CIGS for the RIS to form. Subsequently, if an RIS layer can be grown on top of such a CIGS layer independently of the Cu deficiency, it should be possible to reduce *FF*. In order to test this hypothesis, a second sample set with $CGI = 0.95$ was deposited and covered with an RIS thin film with varied thickness. Fig. 5 shows the Rb distribution in these samples compared with a sample with an RbF-PDT before and after etching in diluted ammonia.

As one can see, the Rb profiles of the RIS set are almost not altered by the ammonia etching, while the residual Rb is completely removed from the PDT sample. Since RIS is stable under ammonia etching [11], we therefore conclude that the deposition of a stable RIS phase on top of the CIGS was successful. Fig. 6 shows the PV parameters measured on this sample set. After an initial increase of *FF* due to the steadily increasing V_{OC}, the blocking behavior of the RIS layer is leading to a rather strong decrease in *FF*—following the model described earlier.

We attribute the steadily increasing V_{OC} with thicker RIS layers to the fact that Rb is diffusing into the bulk of the CIGS absorbers during the RIS deposition, which is done at elevated temperature (530 °C compared with 280 °C in case of the PDT). This is in agreement with the fact that we do measure improved bulk properties (e.g., carrier concentration, not shown here) on these samples as well. This tradeoff of increasing V_{OC} and decreasing *FF* with thicker RIS layers leads to an optimum efficiency at about 4 min RIS deposition, which is substantially shorter than the RbF-PDT, which takes 15 min. Note that the slight differences in j_{SC} are within the error of the measurement. The *EQE* (not shown) does not show any trend with increasing RIS thickness.

Another advantage of the direct RIS deposition is shown in Fig. 7. While the RbF-PDT leads to a roll over at high bias voltages, as it was already described before [16], the RIS deposition does not lead to such a behavior. In case of the RbF-PDT, the roll over was explained by a strong Na depletion near the back contact due to the exchange mechanism of Na and Rb on samples with $CGI = 0.9$ [16]. As can be seen in the GD-OES depth profiles of Na shown in Fig. 8, this Na depletion due to the PDT is also valid in case of CIGS grown with $CGI = 0.95$. The RIS deposition does not lead to such an Na depletion and therefore to

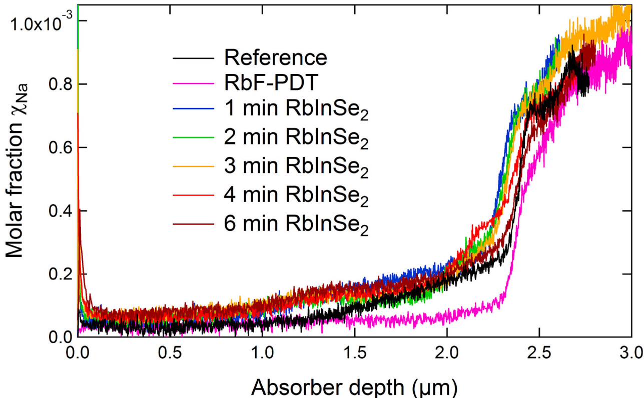

Fig. 8. Na depth profiles as measured by GD-OES.

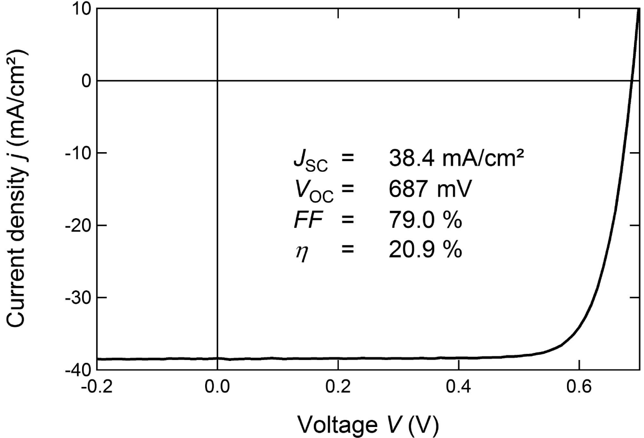

Fig. 9. PV parameters of the best cell with ARC and photolithographic grid. The sample is from the run with 4 min RIS deposition.

the formation of a back contact barrier and the correlated current blocking at high bias voltages. We assume that this is due to the fact that the RIS is deposited at much higher temperatures than the PDT leading to a compensation of the Na depletion near the back contact by additional Na diffusing from the glass into the CIGS during the RIS deposition.

Finally, a substrate of the run with 4 min RIS deposition was used to prepare optimized solar cells using a photolithographic deposited grid as well as photolithographic cell separation and subsequent deposition of an antireflective coating with $\mathrm{MgF_2}$. The j–V curve of the best cell of this substrate is shown in Fig. 9. The high efficiency of 20.9% (in-house measurement) demonstrates that the RIS deposition, although detrimental to *FF*, can be a fast alternative to the conventional RbF-PDT.

V. Conclusion

We could show that varying the *CGI* of CIGS absorber layers has decisive impact on the effectiveness of an RbF-PDT performed subsequently to the absorber growth. This effect is strongly related to the presence of a Cu deficiency at the surface of the CIGS thin film, hence the availability of Cu vacancies for the Rb atoms to occupy. We propose a model following which the carrier concentration is only increased by the Rb–Na exchange mechanism, if the amount of available $\mathrm{V_{Cu}}$ is limited ($CGI \geq 0.8$). Furthermore, the PDT leads—according to that model—to the formation of an RIS layer at the Cu-depleted surface up to *CGI* of about 0.9 reducing *FF*. Only on absorbers grown very close to stoichiometry (e.g., $CGI = 0.95$), the formation of the RIS layer can be suppressed leading to a recovery of the *FF*. This behavior and the fact that different *CGI*s are used in different laboratories could be an explanation for the discrepancy in the results reported regarding the effects of the RbF-PDT on *FF*, which was mentioned in the introduction. The fact that the direct RIS deposition on samples with $CGI = 0.95$ again leads to a lowered *FF*, although the RbF-PDT did not, is strongly supporting the described model. However, although the RIS layer leads to this detrimental effect, it could be used as a fast alternative for the RbF-PDT, since it can be performed faster and leads to overall improved efficiency compared with the Rb-free reference device.

Acknowledgment

The authors would like to thank B. Bunn, M. Hartig, K. Mayer-Stillrich, J. Lauche, T. Münchenberg, I. Dorbandt, S. Stutzke, and M. Kirsch for preparation of the substrates and finishing of the solar cells, C. Klimm for the SEM-EDX measurements, S. Zahedi-Azad for the close collaboration regarding GD-OES as well as R. Klenk and R. Scheer for fruitful discussions. Furthermore financial support by the German Federal Ministry for Economic Affairs and Energy in the frame of the speedCIGS project (contract number 0324095D) is appreciated.

References

[1] A. Chirilă *et al.*, “Potassium-induced surface modification of Cu(In,Ga)Se2 thin films for high-efficiency solar cells,” *Nature Mater.*, vol. 12, pp. 1107–1111, Nov. 2013.

[2] P. Jackson *et al.*, “Effects of heavy alkali elements in Cu(In,Ga)Se2 solar cells with efficiencies up to 22.6%,” *Physica Status Solidi Rapid Res. Lett.*, vol. 10, pp. 583–586, Jul. 2016.

[3] T. Kato, J.-L. Wu, Y. Hirai, H. Sugimoto, and V. Bermudez, “Record efficiency for thin-film polycrystalline solar cells up to 22.9% achieved by Cs-treated Cu(In,Ga)(Se,S)2,” *IEEE J. Photovolt.*, vol. 9, no. 1, pp. 325–330, Jan. 2019.

[4] P. Pistor *et al.*, “Experimental indication for band gap widening of chalcopyrite solar cell absorbers after potassium fluoride treatment,” *Appl. Phys. Lett.*, vol. 105, Jul. 2014, Art. no. 063901.

[5] T. P. Weis *et al.*, “Injection current barrier formation for RbF postdeposition-treated Cu(In,Ga)Se2-based solar cells,” *Adv. Mater. Interfaces*, vol. 5, Feb. 2018, Art. no. 1701007.

[6] S. Ishizuka *et al.*, “Group III elemental composition dependence of RbF post deposition treatment effects on Cu(In,Ga)2 thin films and solar cells,” *J. Physical Chemistry C*, vol. 122, pp. 3809–3817, Jan. 2018.

[7] S. Zahedi-Azad, M. Maiberg, R. Clausing, and R. Scheer, “Influence of heavy alkali post deposition treatment on wide gap Cu(In,Ga)Se2,” *Thin Solid Films*, vol. 669, pp. 629–632, Jan. 2019.

[8] T. Lepetit, G. Ouvrard, and N. Barreau, “KF post deposition treatment in co-evaporated Cu(In,Ga)Se2 thin film solar cells: Beneficial or detrimental effect induced by the absorber characteristics,” *Prog. Photovolt., Res. Appl.*, vol. 25, pp. 1068–1076, Dec. 2017.

[9] M. D. Heinemann *et al.*, “Evolution of opto-electronic properties during film formation of complex semiconductors,” *Scientific Rep.*, vol. 7, Apr. 2017, Art. no. 45463.

[10] R. Scheer, A. Neisser, K. Sakurai, P. Fons, and S. Niki, “$\mathrm{Cu(In_{1-x}Ga_x)Se_2}$ growth studies by in situ spectroscopic light scattering,” *Appl. Phys. Lett.*, vol. 82, pp. 2091–2093, Mar. 2003.

[11] T. Kodalle *et al.*, “Properties of co-evaporated $RbInSe_2$ thin films,” *Physica Status Solidi Rapid Res. Lett.*, vol. 13, Mar. 2019, Art. no. 1800564.

[12] T. Kodalle *et al.*, “Glow discharge optical emission spectrometry for quantitative depth profiling of thin-film chalcopyrite layers,” *J. Analytical At. Spectrom.*, vol. 34, pp. 1233–1241, 2019, doi: 10.1039/c9ja00075e.

[13] M. Burgelman, P. Nollet, and S. Degrave, “Modelling polycrystalline semiconductor solar cells,” *Thin Solid Films*, vol. 361–362, pp. 527–532, Feb. 2000.

[14] M. Gloeckler, A. L. Fahrenbruch, and J. R. Sites, “Numerical modelling of CIGS and CdTe solar cells: Setting the baseline,” in *Proc. 3rd World Conf. Photovolt. Energy Convers.*, vol. 1, May 2003, pp. 491–494.

[15] A. Vilalta-Clemente *et al.*, “Rubidium distribution at atomic scale in high efficient $Cu(In,Ga)Se_2$ thin-film solar cells,” *Appl. Phys. Lett.*, vol. 112, Mar. 2018, Art. no. 103105.

[16] T. Kodalle *et al.*, “Elucidating the mechanism of an RbF post deposition treatment in CIGS thin film solar cells,” *Sol. Rapid Res. Lett.*, vol. 2, Sep. 2018, Art. no. 1800156.

[17] R. Wuerz, W. Hempel, and P. Jackson, “Diffusion of Rb in polycrystalline $Cu(In,Ga)Se_2$ layers and effect of Rb on solar cell parameters of $Cu(In,Ga)Se_2$ thin-film solar cells,” *J. Appl. Phys.*, vol. 124, Oct. 2018, Art. no. 165305.

[18] S. Karki *et al.*, “Analysis of recombination mechanisms in RbF-treated CIGS solar cells,” *IEEE J. Photovolt.*, vol. 9, no. 1, pp. 313–318, Jan. 2019.

[19] P. Schöppe *et al.*, “Rubidium segregation at random grain boundaries in $Cu(In,Ga)Se_2$ absorbers,” *Nano Energy*, vol. 42, pp. 307–313, Dec. 2017.

[20] R. Caballero *et al.*, “Investigation of $Cu(In,Ga)Se_2$ thin film formation during the multi-stage co-evaporation process,” *Prog. Photovolt., Res. Appl.*, vol. 21, pp. 30–46, Jan. 2013.

[21] N. Maticiuc *et al.*, “In vacuo XPS investigation of $Cu(In,Ga)Se_2$ surface after RbF post deposition treatment,” *Thin Solid Films*, vol. 665, pp. 143–147, Nov. 2018.

[22] C. Rincon *et al.*, “Raman spectra of the ordered vacancy compounds $CuIn_3Se_5$ and $CuGa_3Se_5$,” *Appl. Phys. Lett.*, vol. 73, pp. 441–443, Jul. 1998.

[23] P. Schöppe *et al.*, “Overall distribution of Rubidium in highly efficient $Cu(In,Ga)Se_2$ solar cells,” *ACS Appl, Mater. Interfaces*, vol. 10, pp. 40592–40598, Nov. 2018.

[24] M. Chugh, T. D. Kühne, and H. Mirhosseini, “Diffusion of alkali metals in polycrystalline $CuInSe_2$ and their role in the passivation of grain boundaries,” *ACS Appl. Mater. Interfaces*, vol. 11, pp. 14821–14829, Apr. 2019.

[25] T. Feurer *et al.*, “RbF post deposition treatment for narrow bandgap $Cu(In,Ga)Se_2$ solar cells,” *Thin Solid Films*, vol. 670, pp. 34–40, Jan. 2019.

[26] R. Kormath Madam Raghupathy, T. D. Kühne, G. Henkelman, and H. Mirhosseini, “Alkali atoms diffusion mechanism in $CuInSe_2$ explained by kinetic Monte Carlo simulations,” *Adv. Theory Simul.*, vol. 2, 2019, Art. no. 1900036, doi: 10.1002/adts.201900036.

[27] M. Malitckaya, H.-P. Komsa, V. Havu, and M. J. Puska, “Effect of alkali metal atom doping on the $CuInSe_2$-based solar cell absorber,” *J. Physical Chemistry C*, vol. 121, pp. 15516–15528, Jul. 2017.